DOI: 10.13009/EUCASS2025-224
11TH EUROPEAN CONFERENCE FOR AERONAUTICS AND SPACE SCIENCES (EUCASS)

Experimental Investigation of Thin Liquid Films for Liquid Rocket Propulsion

Federico Giambelli[⋆]*, Alessio Nisticò*[⋆]*, Giulia Rondena*[⋆]*, Francesco Calabrò*[⋆]*, Roberto Pistone Nascone*[⋆]*,*
Christian Paravan[⋆†]*, Martina Formidabile* [⋆⋆] *and Michele Urbano Martini* [⋆⋆]
[⋆]*Department of Aerospace Science and Technologies, Politecnico di Milano*
34, Via Giuseppe La Masa, I-20156, Milan, (MI)
[⋆⋆]*AVIO s.p.a*
Via Ariana, I-00034 Colleferro (RM)
federico.giambelli@polimi.it · alessio.nistico@polimi.it · giulia.rondena@mail.polimi.it ·
francesco2.calabro@mail.polimi.it · roberto.pistone@mail.polimi.it · christian.paravan@polimi.it ·
Martina.Formidabile@avio.com · micheleurbano.martini@avio.com
[†]Corresponding author

Abstract

Liquid film Cooling (LFC) is a thermal control strategy for liquid rocket engines (LREs): a thin liquid layer of coolant is injected at the engine walls, shielding them from the intense heat transfer from the propellant stream. The coolant flow is shear-driven by the strong momentum of the engine core stream, and this possibly leads to the onset of hydrodynamic instability. Waves form at the coolant-propellant stream interface, and droplets may detach from the liquid layer to be entrained in the propellant stream. This hydrodynamic instability jeopardises the liquid layer cooling process, since the coolant mass is depleted without being heated to vaporisation. This work aims at investigating the film stripping phenomenon from the liquid coolant under momentum flux conditions similar to those encountered in LREs. An experimental campaign is designed and performed on a purpose-developed test rig. The generation of waves at the film surface and its instability onset are studied by means of high-speed imaging techniques. Then, the experimental findings are compared with the outputs of a 1D numerical code with a detailed entrainment model, assessing the roll-waves frequency and amplitude. The outputs of the study extend current understanding of wave dynamics and entrainment mechanisms, supporting the development of more accurate design tools for LFC systems.

1. Introduction

In liquid rocket engines (LREs), tight control of the heat transferred from the propellant flow to the engine walls is crucial for efficient system design. Therefore, advanced thermal control modelling and strategies shall be implemented. Depending on the mission needs, either active or passive cooling techniques may be adopted in the design. Among active cooling methods, regenerative cooling (RC) plays a central role, and today this is even emphasised by the growing possibilities offered by additive manufacturing. More recently, film cooling (FC) has gained renewed interest in propulsion applications due to (*i*) reduced implementation complexity over RC, (*ii*) relatively small coolant mass flow rates required for effective heat transfer reduction.[11] Moreover, coupling RC with FC is a viable solution to further enhance the cooling capabilities and durability of LREs from the perspective of re-usable systems.

In LFC, a thin liquid layer is injected over the thrust chamber and/or nozzle walls. Given the strong momentum of the propellant stream, the coolant undergoes a shear-driven motion regime. The liquid layer shields the engine walls from the intense enthalpy transfer from the core stream. The propellant flow heats the coolant from the injection temperature to its boiling point by convection and radiation. Once the vaporisation temperature of the coolant is reached, the film provides further protection to the engine walls by the so-called *convective heat transfer blockage*.[4,14] The latter is, in turn, due to the transverse mass blowing in the propellant stream, curtailing the convection mode. The thermal protection of the coolant layer is guaranteed as far as the hydrodynamic instability onset is prevented. Film stability is crucial to avoid jeopardising the reduction in the heat fluxes toward the engine wall. Given the weak momentum of the film, its motion is mainly driven by the dragging effect of the core stream. A velocity gradient is present between the core stream and the liquid film. Thus, the shear stress between the propellant flow and the coolant layer possibly

DOI: 10.13009/EUCASS2025-224

leads to the formation of waves at the liquid layer surface. From these waves, the detachment of liquid droplets, a phenomenon known as *entrainment*, can be triggered.[2,3,6]
The reduction of the liquid film mass due to hydrodynamic instability onset has a strong negative impact on FC shielding action. Yet, few FC models target an evaluation of entrainment mass transfer. Reduction in the Liquid Film Cooled Length (FCL) up to 20 % are reported by Giambelli et al.,[3] when entrainment and its inception criterion are considered and modelled. In this latter work, the entrainment onset criterion by Gater et al.[2] is combined with a correlation for the estimation of entrainment mass loss by Karabeyoglu et al.[7]
In the analysis performed in Ref.,[3] the information on liquid layer stability comes from the heritage developed in hybrid rocket propulsion.[7] Similarly, open-literature studies dealing with liquid film layer stability in propulsion applications come from analyses on liquefying fuel behavior in hybrid rockets. Petrarolo et al.[12] investigated the melted paraffin stripping phenomenon in a hybrid rocket engine with a flat plate configuration. The wavy motion generation at the film surface and the possible onset of instability are studied by high-speed imaging techniques, and experimental results were compared with the Kelvin-Helmholtz stability analysis. In the study, high-speed recordings are processed via Proper Orthogonal Decomposition (POD) to retrieve the most energetic modes for film surface oscillation frequencies and wavelengths.

This work aims at a comprehensive discussion of surface instability onset in these liquid layers operating in shear flow for LRE applications. Experimental investigations (cold flow tests) are combined with the *Py-SFC-1D* modelling. The simulation targets capturing the most relevant features of the liquid motion with a light, simple, but reliable code for fast analysis of different configurations.

The experimental study is based on high-speed recordings, which are processed via an automatic algorithm, similar to that of Petrarolo et Al.[12] The most energetic and periodic modes are, in turn, extracted by the liquid-gas interface tracking and using a Fast Fourier Transform (FFT). The measured oscillation frequencies are then compared with the ones predicted by Py-SFC-1D. The simulation tool provides (*i*) FCL, (*ii*) evaluation of the coolant mass loss by boiling and entrainment, and (*iii*) determination of the oscillation frequencies and wavelengths of the waves formed on the liquid layer surface.

2. Film Cooling Work Principle: Liquid Layer Instability and Entrainment

As previously discussed, liquid layer hydrodynamic stability is a key point when designing liquid-film cooled systems. The onset of hydrodynamic instability in the coolant layer has negative impacts on the film cooling effectiveness, hence drastically reducing the FCL. Giambelli et al.[3] evaluate the reduction in FCL due to entrainment: variations in model predictions in the range −12% to −20% are reported when simulating representative data from the open literature.[8,9,11] Gater et al.[2] provided experimental evidence on entrainment controlling parameters, and their work was used for the validation of the liquid layer stability sub-model of Py-SFC-1D. In Py-SFC-1D, entrainment mass transfer is triggered when an entrainment-related parameter (X_e) overcomes an experimentally defined threshold. A linear fit of the experimental data is used to determine the threshold value, which is given as[2]

$$X_e = \frac{P^{0.5}}{\sigma}\left(\frac{T}{T_{sat}}\right)^{0.25} \tag{1}$$

In Equation 1, P is the dynamic pressure of the core stream, σ is the surface tension of the coolant (under the given operating conditions), T is the temperature of the gas in the core flow and T_{sat} is the saturation temperature of the liquid coolant. Starting from Equation 1, an appreciable entrainment onset threshold is identified by Gater et al.[2] for $X_e \geq 950 - 1000\, lb_f^{-0.5}$. Thus, the entrained mass flux transfer (from the mass per unit of wet perimeter, Γ_l) is expressed as[3] (in SI units):

$$\dot{m}''_{ent} = 1.41 \cdot 10^{-3}(X_e - 474.14)\Gamma_l \tag{2}$$

The entrainment onset is the consequence of a series of events following coolant layer development. First, the surface of the liquid layer undergoes wave formation. The characteristics of these waves, known as *Primary Kelvin-Helmholtz Instabilities* (PKHI), are influenced by the dynamic pressure of the core stream and the momentum difference between the core stream and the surrounding shear layer.[1,12] As the shear stresses exerted over the liquid layer overcome the retaining forces of the latter (i.e., the surface tension), the liquid mass transfers into the gaseous stream by droplets and ligaments, which are classified as *secondary Kelvin-Helmholtz instabilities* (SKHI).[1,12] Thus, the PKHI is a necessary but not sufficient condition for entrainment to occur. In this respect, the entrainment process

DOI: 10.13009/EUCASS2025-224

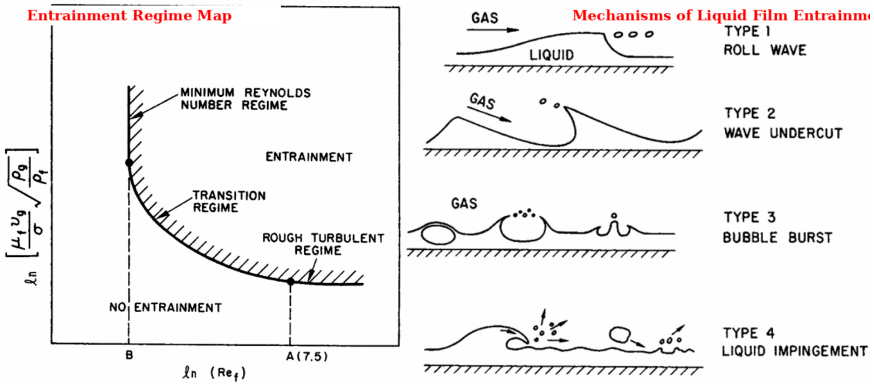

Figure 1: Regimes for entrainment onset and development (on the left) and schematics of droplet formation dynamics (on the right). The image is adapted from Ishii and Grolmes, 1975.[6]

in liquid films has been widely studied, and different empirical and semi-empirical correlations have been postulated to evaluate critical conditions for the onset of significant droplet mass transfer.[1] In the experimental work of Ishii and Grolmes,[6] a strong correlation between film Reynolds number (Re_f) and gas flow velocity is reported. For which the following definition is given:

$$Re_f = \frac{4\,\Gamma_l}{\mu_l} \tag{3}$$

Where the Γ_l stands for the liquid mass flow rate per unit of wet perimeter and μ_l is the liquid layer dynamic viscosity. Based on this, Ishii and Grolmes identify three distinct entrainment mass transfer regimes. In the first one, no entrainment occurs due to the extremely limited film Reynolds number ($Re_f < 160$). In the second regime, known as laminar-to-turbulent transition ($160 < Re_f < 1600$), the critical gas velocity is a function of the Re_f and the droplet detachment pattern is dominated by the tearing of the crests of the roll waves. In the third regime, named the *fully turbulent regime* ($Re_f > 1600$), the critical gas velocity is independent of the Re_f and the detachment pattern is dominated by the roll wave mechanism. The Figure 1 provides a schematic representation of the three regimes as a function of the Re_f, and of the possible droplet formation mechanisms experimentally observed after entrainment onset.

In addition to experimental investigations, theoretical analyses are also performed. As discussed by Petrarolo,[12] the critical gas velocity for the onset of PKHI can be estimated by domain geometry, gas properties and flow conditions. A $2D$, viscous-bounded model can be used to study the stability of stratified gas–liquid flows (see Figure 2). The governing equations are the continuity and momentum balances, written under the following assumptions:

- The liquid film is thin and incompressible, with constant density ρ_l and viscosity μ_l;
- The gas phase is compressible, with density ρ_g and viscosity μ_g;
- A no-slip condition is imposed to the upper wall;
- A kinematic condition based on normal stress balance is imposed for the interface between phases.

Equations are linearised, applying a sinusoidal perturbation to the liquid film thickness $h(x,t)$ as:

$$h(x,t) = A\,\exp\left(i\kappa x - i\omega t\right) \tag{4}$$

The complex wave number κ provides insight into the spatial stability of the system. The complex wave frequency ω defines the temporal stability of the system. Spatial instability is indicated by a positive imaginary part of the wavenumber, while temporal instability corresponds to a positive real part of the frequency. Solving the perturbed equations, the following dispersion relation is obtained:

$$K_0\omega^2 + 2K_1\omega + K_2 = 0 \tag{5}$$

where the coefficients K_0, K_1 and K_2, are defined as:

$$K_0 = a_g\rho_g + a_l\rho_l \tag{6}$$

DOI: 10.13009/EUCASS2025-224

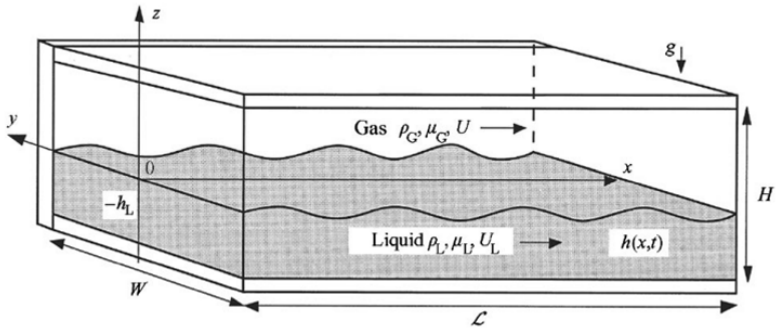

Figure 2: 2D domain for the derivation of stability equations. The image is taken from Petrarolo, 2020.[12]

$$K_1 = -\kappa U a_g \rho_g + i\kappa^2 \left(a_g \mu_g + a_l \mu_l\right) \tag{7}$$

$$K_2 = -2iU a_g \mu_g \kappa^3 + \left(U^2 \kappa^2 a_g \rho_g - \kappa g_0 \left(\rho_l - \rho_g\right) - \sigma \kappa^3\right) \tag{8}$$

In the Equation 6-Equation 8, the following nomenclature is used: $a_l = \coth(\kappa h_l)$, $a_g = \coth(\kappa h_g)$, $\rho = \rho_l/\rho_g$ and $\beta = \sqrt{\frac{\sigma}{g_0 \rho_l}}$. Being: ρ the fluid densities, μ their viscosities, h their thicknesses, σ the liquid surface tension, and g_0 the gravity acceleration. Also, the subscripts l and g stand for "liquid" and "gas", respectively. In this respect, the critical velocity is defined as:

$$U_{crit}^2 = g_0 \frac{\left(a_l \mu_l + a_g \mu_g\right)^2}{a_l a_g^2 \mu_g^2 + \rho a_g a_l^2 \mu_l^2} \left(\beta^2 \kappa + \frac{1-\rho}{\kappa}\right) \tag{9}$$

3. Experimental Logic and Methods

This section describes the experimental logic of the work. The objective of this study, as reported in the section 1, is a detailed analysis of the entrainment onset and of the surface wave features. Observable parameters of interest are defined based on the analysis of Berna et al.[1] The experimental observations are used to further validate Py-SFC-1D.
In this section, the first part of the discussion follows open-literature studies on liquid film cooling. The test rig is described considering (*i*) hardware features and implementation, and (*ii*) data acquisition procedures. The experimental setup is designed to visualise the surface layer hydrodynamic instability onset of a coolant flow in a shear flow. A cold stream of nitrogen flows over the liquid layer, possibly leading to hydrodynamic instability phenomena. The windowed facility enables high-speed recording of the surface wave formation and of droplet detachment.
Based on the works of Berna et al.,[1] Rayana et al.,[13] and Petrarolo et al.,[12] the wavy motion of the liquid-gas interface of a shear flow is analysed to assess: the oscillation frequency, the wavelength and wave-related parameters as waveshape and wave celerity. Details on the determination of each parameter are reported in the original Reference,[1] while Figure 3 provides a schematic defining all the relevant parameters.

The celerity of the wave (c) is the velocity of the flowing surface wave. Marmottant and Villermax,[10] from a theoretical study on co-axial jets, showing that a shear instability governs the large waves on the jet. The linear shear instability analysis provides the following equation for c:

$$c = \frac{\sqrt{\rho_g} U_g + \sqrt{\rho_l} U_{ls}}{\sqrt{\rho_g} + \sqrt{\rho_l}} \tag{10}$$

In the Equation 10, U_g is the gas stream velocity and U_{ls} is the liquid surface velocity. This equation can be applied only under the assumption of $U_g >> U_{ls}$, and does not consider viscosity effects. Berna et al.[1] modified Equation 10 to relate c with the physical properties of the gas and the liquid, and with the testing conditions,

$$\frac{c}{\frac{\sqrt{\rho_g} U_g + \sqrt{\rho_l} U_{ls}}{\sqrt{\rho_g} + \sqrt{\rho_l}}} \propto Re_g^{-0.38} Re_l^{0.16} C_w^{-0.13} \tag{11}$$

DOI: 10.13009/EUCASS2025-224

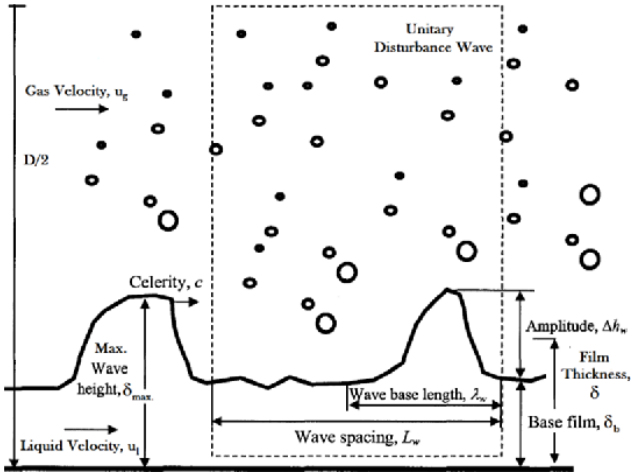

Figure 3: Schematic view of unit disturbance wave, image is taken from Berna et al., 2014.[1]

being Re_g and Re_l the Reynolds numbers of the gas stream and of the liquid layer, and C_w a constant accounting for the effect of σ on the circulation/dissipation flow in the wave.[6] This latter parameter is defined based on the viscosity number N_μ, according to Ishii-Grolmes:[6]

$$N_\mu = \frac{\mu_l}{\rho_l \sigma \sqrt{\frac{\sigma}{g\Delta\rho}}} \tag{12a}$$

$$C_w = 0.028 N_\mu^{-4/5} \qquad \text{for } N_\mu \leq 1/15 \tag{12b}$$

$$C_w = 0.25 \qquad \text{for } N_\mu > 1/15 \tag{12c}$$

In the Equation 12, properties of the fluid as density (ρ_l) and viscosity (μ_l) are introduced, together with $g = 9.81\ m/s^2$. Computing the wavelength of the surface disturbances (λ), as

$$\lambda = \frac{c}{\nu} \tag{13}$$

In the Equation 13, the wave frequency (ν) is defined by the gas-liquid Strouhal number (St_{gl}), as reported by Berna et al.[1] The St_{gl} is related to Re_l, Re_g and to the Eötvös (Eo) number, as:

$$St_{gl} \propto Re_g^{0.53} Re_l^{-0.48} Eo^{0.27} \left(\frac{\rho_g}{\rho_l}\right)^{0.14} C_w^{0.68} \tag{14}$$

with

$$St_{gl} = \frac{\nu D}{\sqrt{U_g U_{ls}}}, \qquad Eo = \frac{gD^2(\rho_l - \rho_g)}{\sigma} \tag{15a}$$

In the hereby presented version, Py-SFC-1D fetures a detailed treatment of the entrainment including: (*i*) the onset criterion from Gater and L'Ecuyer,[2] enhanced by analyses of Ishii and Grolmes,[6] and (*ii*) the capture of the wave features by Berna et al.[1] that is presented in Equation 11-Equation 14.

In this work, four different flow rates of N_2 stream and four different mass flow rates of liquid (H_2O) are investigated. Water is selected as the coolant for its easier implementation. Given the fixed squared section of the testing chamber, the different Nitrogen flow rates are exploited to investigate different dynamic environments. Whereas the effect of the liquid layer mass allows to have an indication of the retaining forces effects, given a core stream dynamic pressure. The following testing conditions are reported in Table 1

DOI: 10.13009/EUCASS2025-224

Test ID.	$\dot{\mathbf{m}}_{\mathbf{N_2}}$ [g s^{-1}]	$\rho\mathbf{u^2}\vert_{\mathbf{N_2}}$ [Pa]	$\dot{\mathbf{m}}_{\mathbf{H_2O}}$ [g s^{-1}]			
			3	6	9	12
			$\mathbf{Re_l}$ [−]			
N2-21-H2O-XX	21	921.60	479.23	958.47	1437.70	1916.93
N2-42-H2O-XX	42	3686.40				
N2-61-H2O-XX	61	7776.13				
N2-66-H2O-XX	66	9103.15				

Table 1: Experimental matrix showing nitrogen mass flow rate ($\dot{m}_{N_2}$), dynamic pressure ($\rho u^2|_{N_2}$), and the corresponding liquid Reynolds number (Re_l) for different water mass flow rates ($\dot{m}_{H_2O}$). Tests are identified as N2-$\dot{m}_{N_2}$-H2O-$\dot{m}_{H_2O}$. Every nitrogen mass flow rate (21 to 66 g/s) is tested for four $\dot{m}_{H_2O}$ (3 to 12 g/s), for a total of 16 test conditions.

3.1 Experimental Logic

A wide series of experimental setups have been implemented for the study of surface instability onset in liquid flows.[2,12,13] The approach followed in this work is similar and stems from the achievements of open-literature studies. The retrieval of the most energetic and periodic modes is extracted employing a Fast Fourier Transform (FFT). The oscillation frequencies of the liquid layer are extracted in different dynamic scenarios and then manipulated to assess the unstable λ, which are compared with the neutrality curves, extracted from Equation 9. The ν are retrieved by sampling in time the positions of the liquid film free surface and of the gas core at fixed positions along the jets.

The experimental findings are further compared with the numerical predictions from the Py-SFC-1D model: the wave-related predictions are retrieved whenever the algorithm detects the onset of entrainment. As final validation, the actual verification of mass loss by entrainment is performed via cross-check with the high-speed recording.

3.2 Experimental Setup

All the stability tests are performed on a dedicated setup. In the experimental facility, the following main parts are identified:

- **Nitrogen Supply Line** is deputed to introduce a gaseous high-velocity stream. The supply of the N_2 flow rate is made via a *M55 Mini-Cori Flow Mass Flow Controller* (MFC-M55) by Bronkhorst;
- **Water Supply Line** that feeds the liquid simulating the coolant. The correct supply of the H_2O stream is made via a dedicated 1.0 mm-diameter injector, and $\dot{m}_{H_2O}$ is regulated by a *M15 Mini-Cori Flow Mass Flow Controller* (MFC-M15) by Bronkhorst;
- **Testing chamber**, a windowed slab-like test chamber with 25 mm x 25 mm squared cross section and length of 350 mm. Windows cover a length of 190 mm downward of the injection section;
- **Data Acquisition (DAQ) and Control System** (*National Instrument NI PXIe-1092 with NI PXIe-886 controller*), providing data sampling and storage for a sensor suite made of 7 strain-gauge pressure sensors (PX359-1KGV by OMEGA), and two 1.0 *mm*-diameter-stem K-type thermocouples (supplied by TC Direct), commanding flowmeters and the high-speed recording of the test (*Phantom v710*).

In Figure 4, a complete overview of the feed lines, the sensor suite and the effective testing chamber is given. Focusing on the Figure 5, a peculiar injection configuration is selected for the N_2 stream and the H_2O one. The latter is placed 75.4 *mm* downstream of the N_2 injection to have a fully developed film prior to the carrier flow development. The peculiar descending ramp-like geometries for the slab chamber and the coolant injector are selected in order to avoid abrupt variations in the duct geometry, thus avoiding any possible insurgence of adverse pressure gradients, which may compromise the correct onset of the liquid layer. A key-feature of the facility is the side window implementation, see Figure 6. Two parallel windows are realized on the slab chamber body. The windows enable visualization and illumination of the test section in the region liquid layer develops in. Windows are realized in PMMA (polymethyl methacrylate).

3.3 Data Acquisition

The data acquisition process involves outputs from sensors capturing pressures of liquids and temperatures of liquid and gaseous reactants, and interfacial phenomena. The details in the pressure and temperature transducers are reported

DOI: 10.13009/EUCASS2025-224

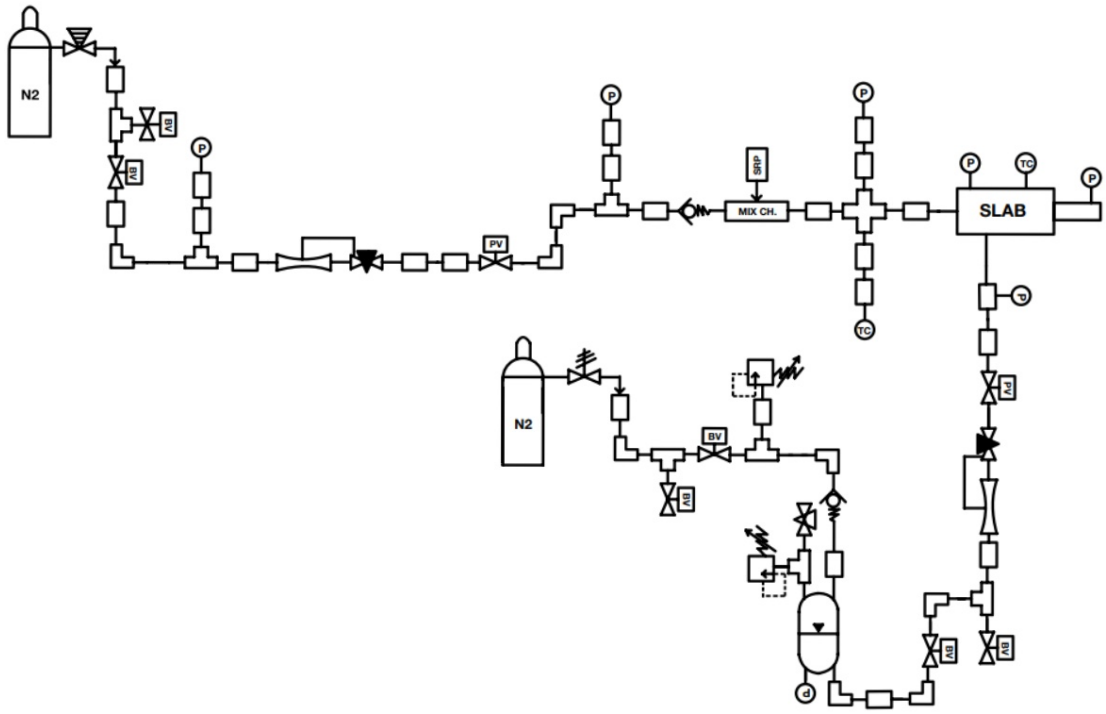

Figure 4: Pipeline and Instrumentation Diagram (P&ID) for the Experimental Apparatus

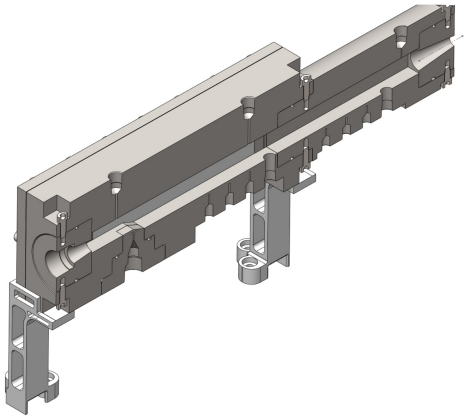

(a) Longitudinal section of Slab Chamber (with an extension duct and nozzle)

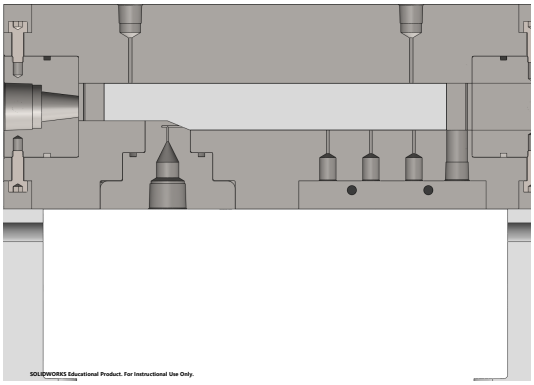

(b) Side view of slab chamber longitudinal section (without extension duct and nozzle).

Figure 5: Slab Chamber sections.

in Table 2. In particular, the relative motion between the liquid and gas phases in the Figure 7 and the interfacial waves are captured by a high-speed camera (Phantom V710). An industrial flashlight provides suitable illumination to the test section. In order to maximise the contrast between the liquid and the N_2 shear flow, illumination is provided from the window opposite to the high-speed camera. In this way, the denser liquid simulating the coolant is shadowed. Videos

DOI: 10.13009/EUCASS2025-224

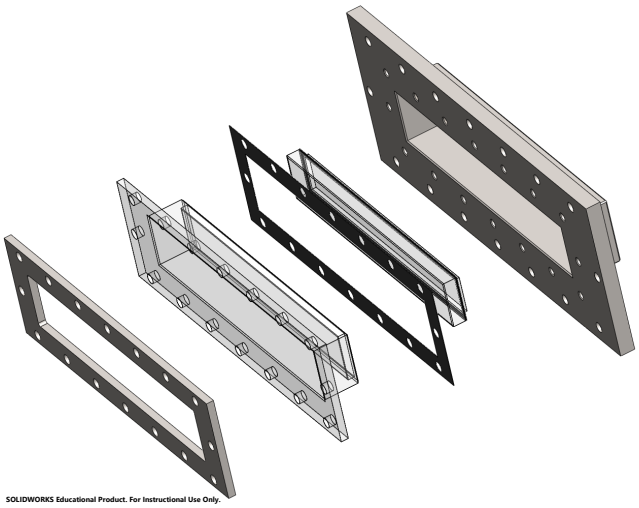

Figure 6: Window sub-assembly exploded view.

are recorded with a frame rate of 1000 fps.

Sensor ID.	**Full Scale**	**Acquisition Rate**, [**Hz**]
M15 Flow Meter	$80\,g/s$ @ $50\,barG$	6.0
M55 Flow Meter	$78\,g/s$ @ $100\,barG$	6.0
PX359-1KGV Press. Sensor	$69\,barG$	1000.0
K-Type Thermocouple, $1.0\,mm$ Stem	$1024\,°C$	10.0

Table 2: Sensor Suite Characteristics

The visualized image shows the liquid layer injector up to the end of the Plexiglass window, for a longitudinal length of $190\,mm$. Possible ruptures of the liquid film length due to dynamic events are more likely in this region, given the higher layer thickness (in turn related to the larger mass flow rate in this region, before any coolant depletion event). The captured image extends vertically showing half of the view occupied by the liquid layer, while the rest is taken by the gaseous stream: generation of waves can be recorded together with the detachment of liquid droplets (see Figure 7).

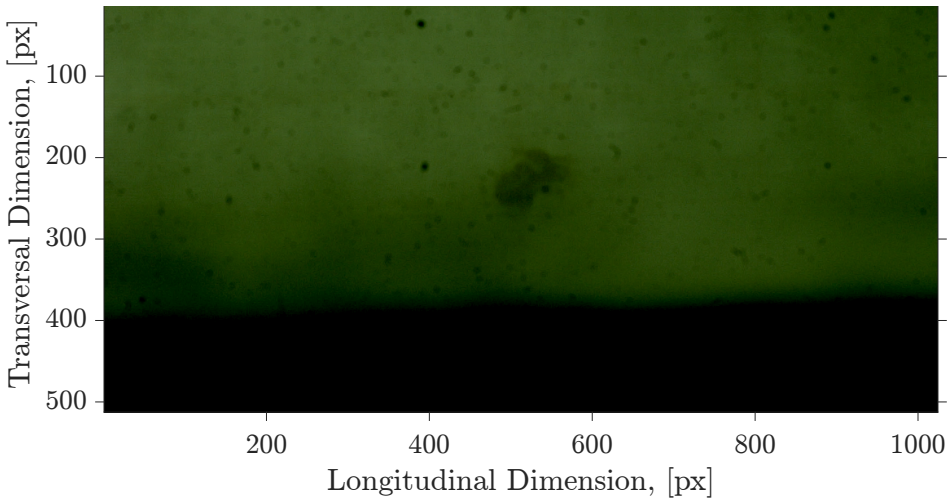

Figure 7: Unprocessed video frame from the high-speed visualisation.

The trigger for the video acquisition is a digital input provided by the BNC-2110 board from NI. The 5 VDC command is supplied to the camera by its trigger, $10\,s$ after reaching a steady state condition in the mass flow meters

DOI: 10.13009/EUCASS2025-224

outputs. The general actuation sequence can be summarized as follows:

- Opening of H_2O pneumatic valve (PV) at t_0 + 2 s;
- Opening of the H_2O mass flow controller (MFC-M15) at t_0 + 4 s;
- Opening of the N_2 PV (PV-N2) at t_0 + 6 s;
- Opening of the N_2 mass flow controller (MFC-M55) at $t_0 + \Delta t_1$. The Δt_1 depends on the $\dot{m}_{H_2O}$. The lower the coolant mass, the longer the delay given by the slow response of the MFC-M15;
- High-speed camera is triggered at $t_0 + \Delta t_2$. The Δt_2 depends on the selected N_2 mass flow rate. The lower the carrier mass flow rate, the longer the delay given by the slow response of the MFC-M55;
- Closing of H_2O flow (MFC-M15) at $t_0 + \Delta t_3$. The Δt_3 is a period of time granting a full steady state condition for the observed phenomenon. In all tested conditions, at least 30 s of steady-state is considered;
- Test sequence ends by closing PV on the H_2O-line, N_2 mass flow controller and PV-N_2. In this sequence, a 2 s buffer separates each event from the following one.

3.4 Data Processing

In this section, the data processing methodology is presented, with a primary focus on video-based analysis. The liquid–gas interface is first extracted from the recorded frames. Subsequently, its temporal evolution is tracked at specific longitudinal positions along the flow domain. For each tested condition, three repetitions are performed to have a sufficiently relevant pool for statistical analysis. For each repetition, three observation windows are considered. The first one starts 3000 frames after the steady state condition is reached for the stream and coolant mass flow rates. The second observation window is taken at half of the test. The third and last analyzed sequence considers the 1000 frames before the end of the steady-state. For each of the three sequences, 301 frames are considered, hence analysing 300 ms of testing. Following this approach led to the investigation of a total of 9 video-sequences for each investigated condition.

3.4.1 Video Analysis and Manipulation

All the video processing is performed via a fully automated MATLAB script, taking as input a batch of video frames and returning the oscillation frequencies for the selected test case. In the script structure, two main operating blocks can be identified: (i) the video processor and (ii) the film-gas interface tracker/analyzer. The former executes the actual editing of the video, while the latter focuses on interface extraction and effective analysis via FFT. In the video-processing phase, the following operations are performed (see Figure 15):

- **Video Grey-Scale**: each frame is converted from the RGB scale (see Figure 8) to the grayscale (Figure 9). This process eases the next step;
- **Video Inversion**: Grayscale frames are inverted, swapping the dark-based pixels with the light ones (see Figure 10);
- **Video Sharpening**: starting from inverted frames, all the contrasts among the liquid and the gaseous phases are sharpened, allowing a better capture of interfacial phenomena, as shown in Figure 11;
- **Video Binarisation**: sharpened frames are now converted into a binary matrix. Each of the points in the (darker) gas region are labelled with 0, whereas the points in the liquid region (resulting in brighter, in the binary image) are marked with 1, as depicted in Figure 12;
- **Interface Extracting**: from the binary matrix, the liquid-gas interface is now recognised as the line of discontinuity between zeros and ones. The Canny method is then exploited (see Figure 13). Interfacial regions may be found inside either the full liquid or the full gas, showing a closed path. Thus, a filtering operation is performed to remove outliers, see Figure 14;
- **Effective Interface Motion Sampling**: This operation allows for monitoring the evolution of the free surface in time.

DOI: 10.13009/EUCASS2025-224

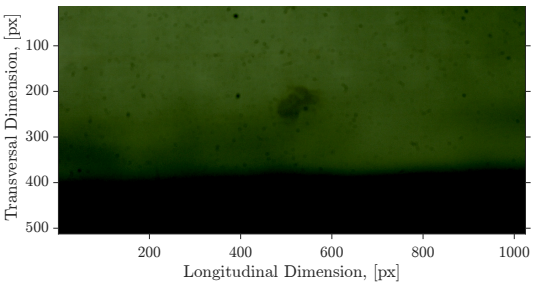

Figure 8: Acquired RGB Unprocessed Frame

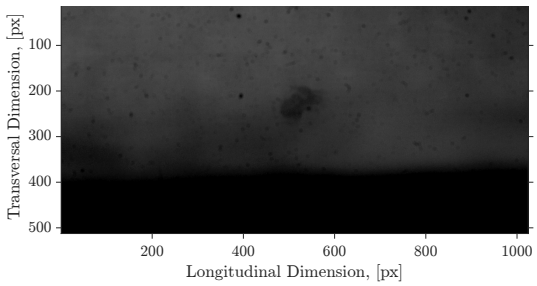

Figure 9: Gray Scale Frame

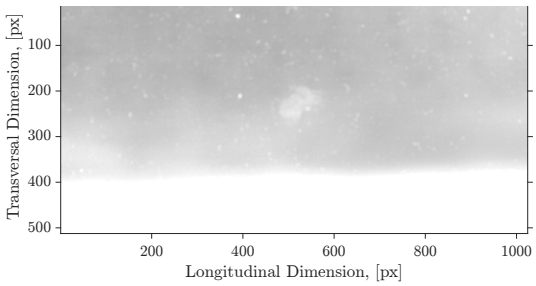

Figure 10: Inverted Gray-Scale Frame

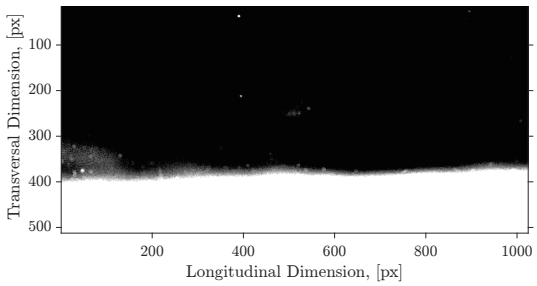

Figure 11: Adjusted Frame

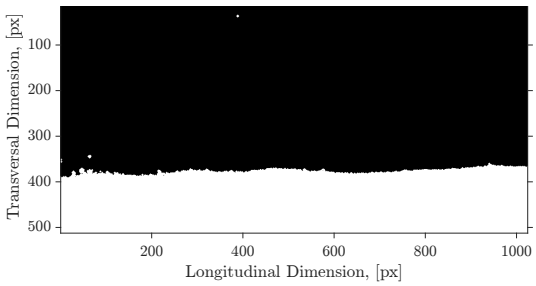

Figure 12: Binarised Frame

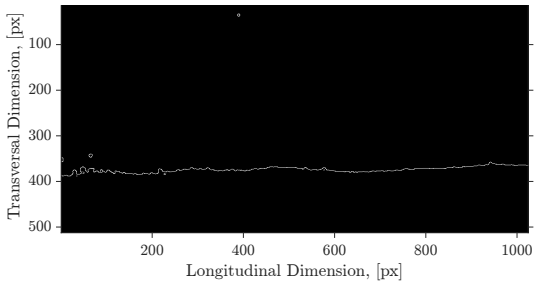

Figure 13: Edge Extraction Frame

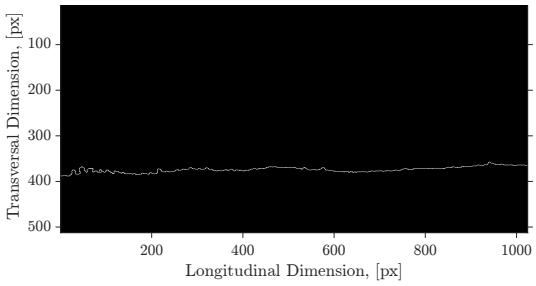

Figure 14: Filtered Edge Frame

Figure 15: Video Processing Procedure

3.4.2 Interface Sampling and Analysis

Relative to the interface evaluation and analysis, nine vertical lines are placed along the longitudinal axis of each frame, serving as floating indicators. The vertical position of the free surface is sampled in time, being identified as the index on the frame spatial matrix. A matrix made of 9x301 elements is created, where the columns represent the analysed frame number, whereas the rows represent the vertical lines exploited for sampling. The frequency content analysis is performed over a single line in time. The single-sided spectrum magnitude of the FFT is assessed and plotted against the frequency array spacing from 0 to 500 Hz (video recording being performed at 1000 Hz). The dominant frequency is then extracted as the one displaying the highest peak in magnitude. Either high or low frequency disturbances can arise as an effect of droplet detachment and higher-order modes, besides Kelvin-Helmholtz. As a consequence, unwanted oscillatory motions have to be identified and discarded. An initial guess for the region of search may be identified by the expected frequency for liquid film oscillations in co-current flows (see Equation 14, and Equation 15a). In addition

DOI: 10.13009/EUCASS2025-224

to this, the frequency content on the pressure signal prior to injection is analyzed, wiping out low-frequency oscillatory motions that are propagated subsequently. Moreover, increasing the operating conditions between tests from low-speed conditions (namely the ones featuring $\dot{m}_{N_2} = 21\ g/s$, see Table 5) upward, the lower limit for film oscillation is set.

4. Results and Discussion

In this section, the results obtained from the video analysis are presented and discussed. The section begins with a brief description of the physical phenomena of relevance under the investigated conditions. This is done to fit the contents of the section 2 to the test conditions encountered during the experimental campaign. Experimental results from the study are then compared with numerical predictions obtained using the Py-SFC-1D model[3] . The analysis proceeds to assess the stability of the liquid film by neutrality curves, from which the critical gas velocity corresponding to the onset of instability is identified. Finally, the experimental evidence of entrainment onset is compared with the numerical predictions, offering a validation of the accuracy of Py-SFC-1D.

4.1 Experimental Phenomenon Analysis

High-speed video recordings of the liquid film behavior show an initial transient regime which is followed by the steady-state condition. A typical early phase-sequence of the test is shown in Figure 18 which clarify the phases the shear-driven motion regime is onset by. At the beginning, the film is rather thick, being the sole fluid entering the slab chamber (see subsection 3.1). As soon as the N_2 gaseous stream enters in the test section, the film looses its surface stability. In this phase, high-amplitude waves featuring the typical roll wave geometry appears at the liquid free surface. Given the operating conditions and the thickness of the liquid layer, large liquid droplets detach from the film. Here, no quantitative assessment on instability may be performed since no organised oscillatory motion is witnessed, the wave generation passes through as an effect of the incoming high-speed gaseous core stream.

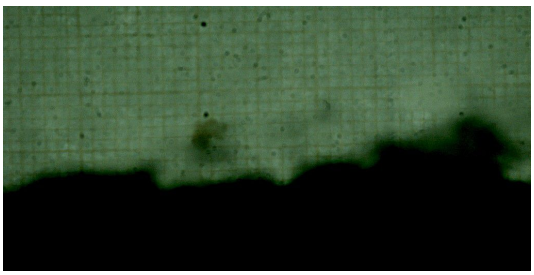

Figure 16: Unprocessed Frame during Transient Induced-Oscillatory Motion at t_0

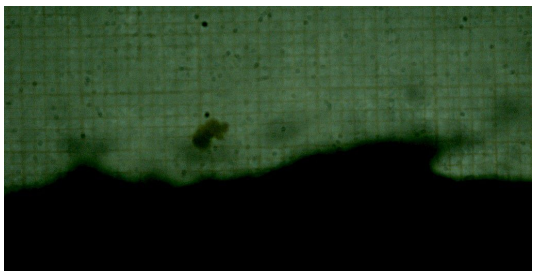

Figure 17: Unprocessed Frame during Transient Induced-Oscillatory Motion at $t_0 + 6\,ms$

Figure 18: Unprocessed Transient Induced Entrainment Regime. Test 1, $\dot{m}_{N_2} = 42\,g/s$, $\dot{m}_{H_2O} = 9\,g/s$.

As the test proceeds, a stretching of the film is observed (see Figure 23): the core stream flow drags the liquid layer by its shearing action. As a consequence, sensible thickness reduction is witnessed in the liquid, since it accelerates by continuity. The observation and measurement time-window starts from here, since the steady-state is reached. The insurgence of oscillatory motion with the possible droplet detachment can be spotted. The tests yield direct observations on the film behavior and the possibility of a relative grading between the different test conditions.

4.2 Experimental Campaign Results: Frequency Content

As discussed in the subsubsection 3.4.2, FFT is used to analyze every test. A single test is described in details here to clarify the outcomes of the data reduction procedure. The test featuring $\dot{m}_{N_2} = 21\,g/s$, and $\dot{m}_{H_2O} = 12\,g/s$ is exploited for this purpose, see Figure 24.

The peak in the Fourier analysis is extracted to be the dominant oscillation frequency for the liquid layer. No dynamic search for the peak is employed. Depending on the selected vertical line along the longitudinal axis, the dominant frequency may shift from the actual expected value to unexpected values. The presence of unexpected modes may derive from the detachment of droplets from the liquid free surface, or from core-stream oscillations. In general, both these phenomena are characterised by a much smaller value than the one corresponding to the dominant oscillation. In these situations, the oscillation frequency is searched within a specific frequency interval, for which the lower limit is set depending on the selected test case and possible flow oscillations.

DOI: 10.13009/EUCASS2025-224

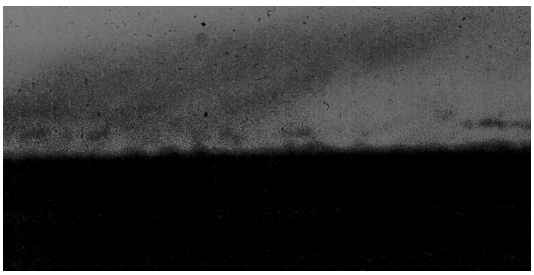

Figure 19: Grey-Scale Frame for Entrainment at Frame: 5535

Figure 20: Grey-Scale Frame for Entrainment at Frame: 5536

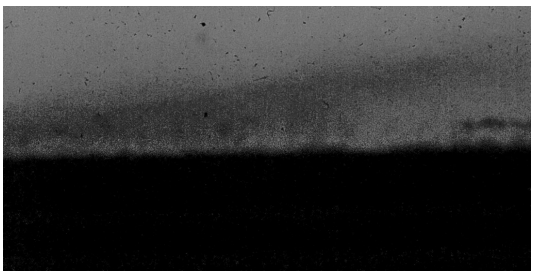

Figure 21: Grey-Scale Frame for Entrainment at Frame: 5826

Figure 22: Grey-Scale Frame for Entrainment at Frame: 5858

Figure 23: Grey-Scale Frames during Steady-State-Induced Entrainment Regime. Test 2, $\dot{m}_{N_2} = 61\,g/s$, $\dot{m}_{H_2O} = 6\,g/s$.

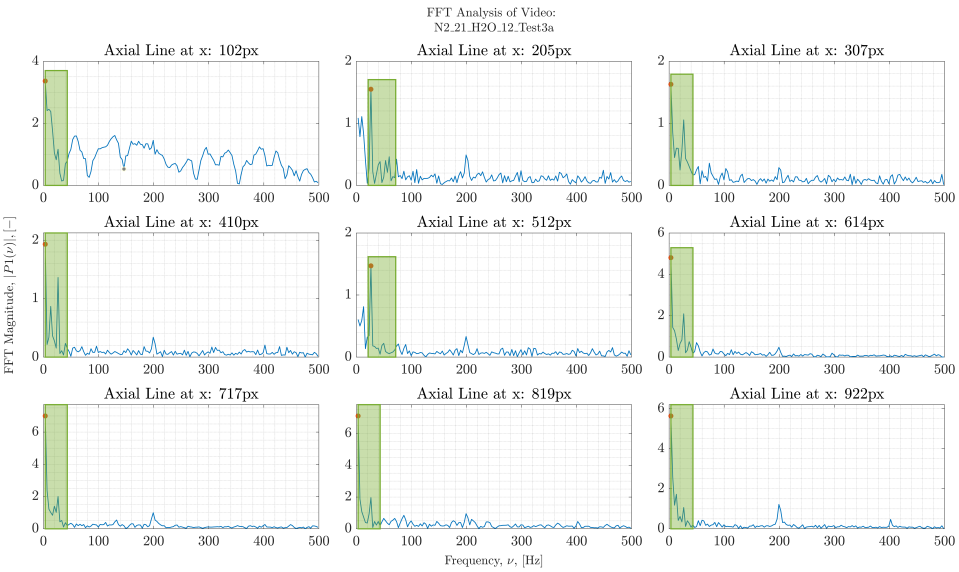

Figure 24: FFT analysis, Test 3, $\dot{m}_{N_2} = 21\,g/s$, $\dot{m}_{H_2O} = 12\,g/s$.

Looking at the results in Table 3, it is possible to notice a very specific trend. At a fixed value of nitrogen stream, the effect of water flow rate is almost negligible. No strong deviation of the oscillation frequencies is reported. Whereas, at a fixed flow rate of water, the effect of the nitrogen stream is highly visible. The dynamic pressure increment coincides with an enhanced trend in the emergence of unstable phenomena, capturing higher oscillation frequencies magnitude. Given the water flow rate insensitivity, for the same value of nitrogen flow rate, an average value of the oscillation frequency is computed. The latter is then compared with the numerical finding, computed with the Py-SFC-1D code, for which minor deviations are reported, attested below the 11.0 %.

At this stage, the experimental wavelengths are retrieved through the surface velocity and the experimental frequency, previously assessed (see section 3). Results from the Py-SFC-1D model can therefore be contrasted with experimental findings, exploiting the Equation 11 and Equation 13.

DOI: 10.13009/EUCASS2025-224

Test ID.	**Exp. Freq.** $[Hz]$	**Avg. Exp. Freq.** $[Hz]$	**Py-SFC-1D Num. Freq.** $[Hz]$	**Rel. Error** $[\%]$
N2-21-H2O-3	35.395	29.15 ± 4.68	32.29 ± 0.19	-10.78
N2-21-H2O-6	25.717			
N2-21-H2O-9	30.085			
N2-21-H2O-12	25.402			
N2-42-H2O-3	61.484	61.62 ± 4.28	66.75 ± 0.39	-8.32
N2-42-H2O-6	60.816			
N2-42-H2O-9	56.909			
N2-42-H2O-12	67.285			
N2-61-H2O-3	94.179	91.35 ± 3.08	98.67 ± 0.59	-8.02
N2-61-H2O-6	88.180			
N2-61-H2O-9	89.238			
N2-61-H2O-12	93.795			
N2-66-H2O-3	108.911	107.71 ± 3.11	107.16 ± 0.63	0.51
N2-66-H2O-6	105.192			
N2-66-H2O-9	111.569			
N2-66-H2O-12	105.186			

Table 3: Experimental results from FFT analysis and comparison with numerical predictions using the Py-SFC-1D model. Grouped values refer to averaged experimental and numerical estimates over each test set.

Test ID.	**Exp. Wavelength** $[mm]$	**Py-SFC-1D Num. Wavelength** $[mm]$
N2-21-H2O-3	149.74	161.40
N2-21-H2O-6	232.92	185.71
N2-21-H2O-9	216.06	200.59
N2-21-H2O-12	272.03	212.80
N2-42-H2O-3	144.75	134.20
N2-42-H2O-6	164.76	150.23
N2-42-H2O-9	190.48	161.89
N2-42-H2O-12	171.06	171.44
N2-61-H2O-3	124.76	119.90
N2-61-H2O-6	149.92	134.08
N2-61-H2O-9	160.02	144.30
N2-61-H2O-12	161.52	152.67
N2-66-H2O-3	114.40	117.17
N2-66-H2O-6	133.18	130.90
N2-66-H2O-9	135.70	140.84
N2-66-H2O-12	152.68	148.98

Table 4: Experimental and numerical wavelength comparison from FFT analysis.

Looking at the results gathered in Table 4, the experimental results validate numerical predictions, especially at higher nitrogen flows. In this case, a double dependency is shown: (i) the effect of $\dot{m}_{N_2}$, at fixed $\dot{m}_{H_2O}$, is to reduce wave spatial repetitions, and (ii) the effect of water mass flow rate enhancement is to induce an enlargement in the oscillation wavelengths. The consequences of an enhanced $\dot{m}_{N_2}$ are to induce more frequent oscillations in both time and space, thus having an instabilizing effect. This finding is supported by previous experimental observations.[12] However, the effect of $\dot{m}_{H_2O}$ seems opposite in trend. At higher $\dot{m}_{H_2O}$ (considering constant testing width), the thickness of the liquid layer and the surface velocity are increased, due to continuity, making the coolant more prone to entrainment onset. At lower coolant flow rates, the oscillations become more frequent in space, as a consequence of the higher velocity gradient between the liquid layer and the gas stream. Conversely, at higher liquid flows, the reduced velocity gradient elongates the roll waves while increasing their amplitude.

4.3 Model Validation and Entrainment Insurgence

At this stage, once the oscillation frequencies and the wavelengths are retrieved, the results are compared with the neutrality curves from Equation 9, assessing whether the system is stable, or not. Considering a viscous-bounded

DOI: 10.13009/EUCASS2025-224

model, the trend of the critical gas velocity, at different wavelengths, is reported in Figure 25.

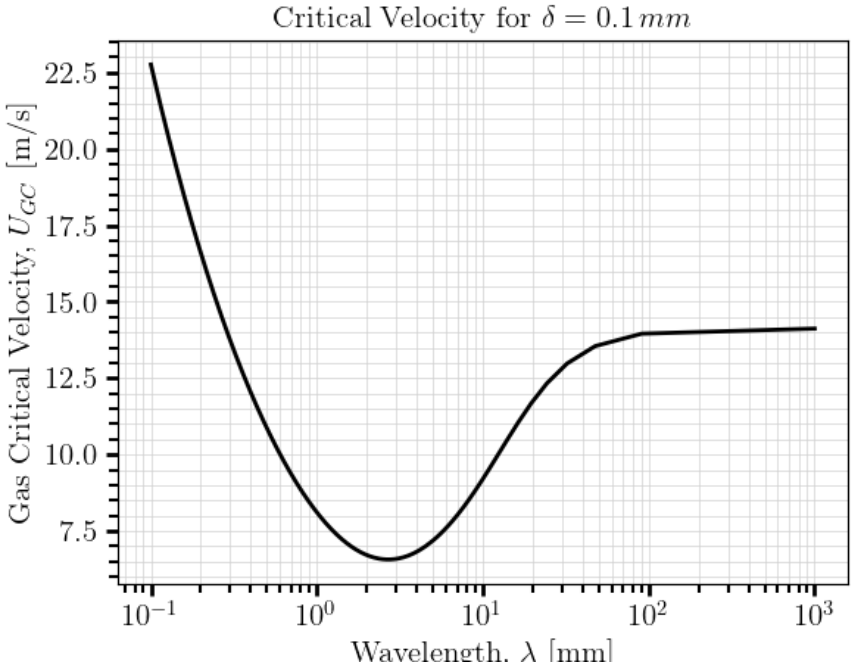

Figure 25: Typical stability curves for critical gas velocity, considering a fixed liquid layer thickness

In the Figure 25, the black curve sets the stability limit for liquid layers. At fixed liquid layer thickness and wavelength, the velocity needed to have an unstable liquid is determined: in a liquid-gas system, the gaseous stream having a velocity above the critical point will induce PKHI, thus provoking an oscillatory motion, from which droplet entrainment may be observed. A system is said to be stable when the gaseous stream travels with a velocity smaller with respect to the critical one. In the Figure 25, a minimum point is found after a monotonic decrease in the curve. From this point onward, the curve is approaching a plateau, as also observed by Ishii et al.[6]

While a single stability curve can be useful to understand a single condition for neutrality, when dealing with an experimental matrix contrasting different operating conditions, a contour-based plot is more convenient to monitor the critical velocity (U_{GC}) as a function of the liquid layer thickness (δ) and wavelength (λ). In Figure 26, the experimental points are plotted against the stability contour. All the 16 tests performed in the analysis are considered, each one highlighted by a marker for the gaseous stream velocity. As can be seen, the tested configurations feature a critical gas velocity well above the actual magnitude of the gas stream. In all investigated conditions, the liquid-gas system exhibits instability onset, since the critical velocity limiting the stable region is in the range $12.0\,m/s$ to $16.0\,m/s$.

The onset of a Kelvin–Helmholtz instability (KHI) mechanism is evidenced both in the plotted data and through visual inspection of high-speed recordings. The latter reveals a pronounced occurrence of unsteady phenomena, including oscillatory motion and the detachment of liquid mass from the free surface. This is confirming the relevance of the Re_f: in all the tested configurations, this parameter ranges above the critical value for the entrainment onset ($Re_f = 160$, as summarised in Table 1).[6] To further substantiate the presence of entrainment, a third verification is performed using the criteria derived from Equation 1 and Equation 2. Following the methodology proposed by Gater et al.,[6] significant entrainment occurs when $X_e > 474.14, \mathrm{N}^{-0.5}$. In all tested cases, besides the ones at $21.0\,g/s$ of nitrogen flow rate, the X_e parameter exceeds this threshold, thereby confirming the occurrence of mass detachment (see Table 5). It should be noted that, under the experimental conditions considered in this work, the tests N2-21-H2O-XX show a X_e value close to the limiting threshold. Yet, in their original research, Gater et al. highlight how $X_e = 474.14\mathrm{N}^{-0.5}$ is a limit for *significant* entrainment insurgence, while reduced instability with small to negligible mass transfer can be experienced also for values below this threshold.

5. Conclusions and Future Developmetns

This work deals with the analysis of cold flow tests on relatively thin liquid layers in shear flow. The investigation is relevant for a deeper insight of liquid coolant film stability in film cooling applications for LREs. The discussed

DOI: 10.13009/EUCASS2025-224

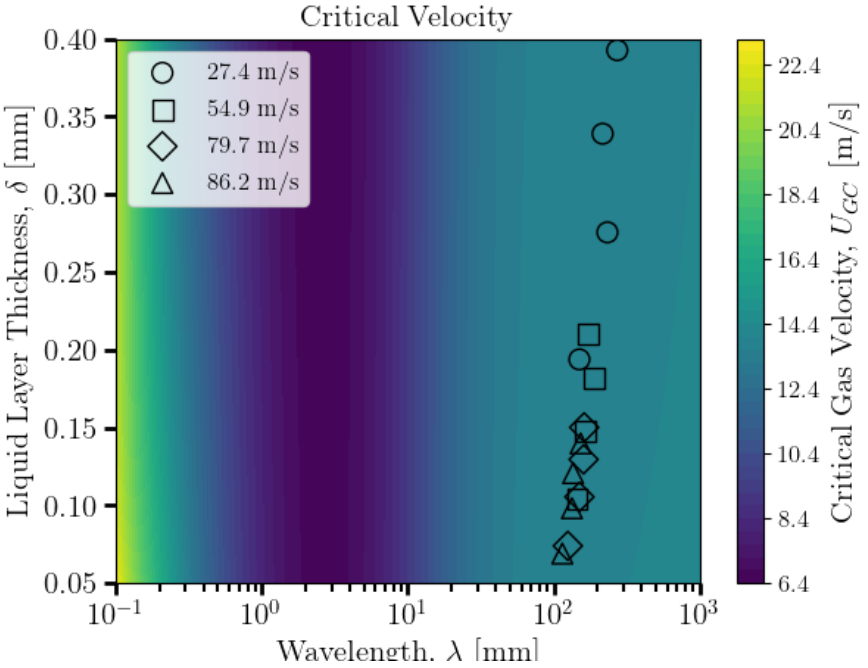

Figure 26: Contour plot for stability, considering also experimental points

Test ID.	$\dot{\mathbf{m}}_{\mathbf{N_2}}$ [g s^{-1}]	$\rho\mathbf{u^2}\vert_{\mathbf{N_2}}$ [Pa]	$\mathbf{X_e}$ [$N^{-0.5}$]
N2-21-H2O-XX	21	921.60	362.52
N2-42-H2O-XX	42	3686.40	725.03
N2-61-H2O-XX	61	7776.13	1053.02
N2-66-H2O-XX	66	9103.15	1139.33

Table 5: Experimental matrix, evaluation of the entrainment-related parameter

results are part of a wider experimental and modeling effort. The presented analysis follows the development of a 1D model for liquid film cooling analysis: Py-SFC-1D.[3] The model simulates the liquid film behavior in shear flow with a hot propellant stream. Based on previous modeling strategies,[5,14] Py-SFC-1D features an extended tracking of the properties of both the coolant and the propellant flow stream. Entrainment mass transfer is modeled, marking a step forward toward a 1D, simplified, yet accurate, liquid film cooling modeling. The validation of the overall Py-SFC-1D is given by Giambelli et al.[3]

The work presented here provides an experimental analysis of liquid film stability that targets a detailed validation of the entrainment modeling presented in Py-SFC-1D. An experimental facility has been designed and implemented to cope with liquid film stability analysis in cold and hot flow conditions, with the former presented here. The facility is windowed, enabling liquid film visualization with the possibility to observe surface wave contours, entrainment mass transfer onset and possible local film inception. Nitrogen is used to simulate the propellant flow, while the liquid phase is water. High-speed visualisations are exploited to track the liquid-shear flow interface. After a proper manipulation to ease interface recognition, recorded images are then analysed by FFT to recognise frequencies in the flow. The wave structure and the entrainment sub-models of Py-SFC-1D, implemented thanks to open-literature efforts[1,6] can therefore be validated against experimental data.

Under the tested experimental conditions (nitrogen mass flow rates in the range 21 to 66 g/s, ambient pressure, water mass flow rates from 3 to 12 g/s) *significant* entrainment is triggered when $X_e \geq 474.14\,N^{0.52}$ (small to negligible droplet mass transfer being possible also below this threshold), as evinced by the high speed recording inquiry. Py-SFC-1D captures entrainment onset, and the implemented modelling of the surface waves shows good agreement with observed frequencies and wavelengths. Achieved results show that, under the investigated conditions, the experimental frequency of the surface waves is caught with a relative error of nearly 11 % for the lowest nitrogen mass flow rate. The performance of Py-SFC-1D improves as the shear flow increases: for nitrogen mass flow rate of 66 g/s, the relative error on wave frequency is of 0.5 %. Similar considerations hold for the wavelength of the surface disturbance, though here both experimental and model results are relatively more scattered. Thus, Py-SFC-1D shows promise in

DOI: 10.13009/EUCASS2025-224

helping earlier phases of liquid film cooling modelling, providing several outcomes of interest (liquid film cooling length, entrainment mass transfer, surface wave properties) with relatively short computational time and good match with experimental evidences.
Future developments of this work include: (*i*) testing under hot flow conditions to evaluate Py-SFC-1D performance with liquid evaporation and a dedicated dataset, (*ii*) inclusion of gaseous film cooling in the model, and (*iii*) CFD analyses under similar operating conditions to provide a complete overview of the liquid film entrainment by experiments, fast yet low-fi modeling (Py-SFC-1D) and high-fidelity CFD simulations.

Acknowledgements

This work is supported by the Italian Space Agency (ASI) by the Contract Nr. 2023-8-I.0, with unique project code (CUP) F83D23000120005, and call identification number 9296180A69. The program is performed in strict collaboration with different entities, all coordinated by AVIO SpA and Finis Terrae SRL.

References

[1] C. Berna, A. Escrivà, J.L. Muñoz-Cobo, and L.E. Herranz. Review of droplet entrainment in annular flow: Interfacial waves and onset of entrainment. *Progress in Nuclear Energy*, 2014.

[2] R. A. Gater and M. R. L'Ecuyer. A fundamental investigation of the phenomena that characterize liquid-film cooling, 1970.

[3] Federico Giambelli, Alessio Nisticò, and Christian Paravan. Liquid film cooling: Advanced modeling and efforts towards validation. *Space Propulsion Conference*, 2024.

[4] W. M. Grissom. Liquid film cooling in rocket engines. Technical report, Morehouse College, 1991.

[5] William M Grisson. Liquid film cooling in rocket engines, 1991.

[6] M. Ishii and M. A. Grolmes. Inception criteria for droplet entrainment in two-phase concurrent film flow, 1975.

[7] M. A. Karabeyoglu, D. Altman, and B. J. Cantwell. Combustion of liquefying hybrid propellants: Part 1, general theory. *Journal of Propulsion and Power*, 18:610–620, 2002.

[8] G. R. Kinney. Internal film cooling experiments with 2- and 4-inch smooth surface tubes and gas temperatures to 2000° f. Technical report, NACA, 1952.

[9] E. L. Knuth. *The Mechanics of Film Cooling*. PhD thesis, California Institute of Technology, 1954.

[10] P.G.M. Marmottant and E. Villermaux. On spray formation. *Journal of fluid mechanics*, 498:73–111, 2004.

[11] G. Morrel. Investigation of internal film cooling of 1000-pound-thrust liquid-ammonia - liquid oxygen rocket-engine. NACA Research Memorandum 1951-E51E05, NACA, Lewis Flight Propulsion Laboratory, Cleveland, Ohio, April 1951.

[12] Anna Petrarolo. Liquid layer combustion instabilities in paraffin-based hybrid rocket fuels. Technical report, Universität Stuttgart, 2020.

[13] Fares Ben Rayana, Alain Cartellier, and Emil J.Hopfingr. Assisted atomzation of a liquid layer: Investigation of the parameters affecting the mean drop size prediction. *ICLASS*, 2006.

[14] S. R. Shine, S. Sunil Kumar, and B. N. Suresh. A new generalised model for liquid film cooling in rocket combustion chambers. *International Journal of Heat and Mass Transfer*, 55:5065–5075, 9 2012.